IEEE Access
Multidisciplinary ⋮ Rapid Review ⋮ Open Access Journal

Received 5 June 2023, accepted 7 July 2023, date of publication 18 July 2023, date of current version 7 August 2023.

Digital Object Identifier 10.1109/ACCESS.2023.3296689

RESEARCH ARTICLE

Multi-Objective Matched Synchrosqueezing Chirplet Transform for Fault Feature Extraction From Marine Turbochargers

FEI DONG[1], JIANGUO YANG[1,2,3], LEI HU[1,2,3], SICONG SUN[1], AND YUNKAI CAI[1]
[1]School of Naval Architecture, Ocean and Energy Power Engineering, Wuhan University of Technology, Wuhan 430063, China
[2]National Engineering Laboratory for Marine and Ocean Engineering Power System, Electronic Control Sub-Laboratory for Low-Speed Engine, Wuhan 430063, China
[3]Key Laboratory of Marine Power Engineering and Technology, Wuhan 430063, China

Corresponding author: Yunkai Cai (caiyunkai@whut.edu.cn)

This work was supported in part by the High-Tech Ship Research Projects from the Ministry of Industry and Information Technology and the Ministry of Finance of China.

ABSTRACT Turbocharger is one of the vital parts of a diesel engine causing a high failure rate. Its surface vibration signal contains important time-varying features. To better process the nonstationary signals with time-varying features and perform the time-frequency transformation on the turbocharger surface vibration signal, a novel multi-objective matched synchrosqueezing chirplet transform method is proposed in this paper. The method is based on the Linear Chirplet Transform to optimize the selection of the demodulation rate. Parameters such as Rayleigh entropy and signal-to-noise ratio are used as targets to select the value of the optimal demodulation rate. Then the local maximum synchrosqueezing transform is used as a post-processing method for time-frequency rearrangement of the signal. This method improves the energy concentration of the transformation result while maintaining the ability of signal reconstruction. On the test stand, the turbocharger fault samples were obtained. The time-domain signals of the turbocharger at the $1\times$, $2\times$, and $9\times$ frequencies were reconstructed based on the time-frequency transformation results, and fault characteristic parameters were extracted from them. Then the effectiveness of the fault feature parameter identification ability was validated by Principal Component Analysis. The study showed that our proposed MOMSSCT method's transformation results have high time-frequency energy aggregation, clear trajectories, and a 37.5% reduction in frequency spread width. The extracted fault characteristic parameters have good fault classifiability under various turbocharger operating conditions. Using the fault features extracted by MOMSSCT, the diagnostic accuracy rate can reach more than 85%.

INDEX TERMS Fault feature parameter extraction, time-frequency transformation, turbocharger.

I. INTRODUCTION

As one of the crucial components of marine diesel engines, the turbocharger experiences difficult working conditions. It is easy to fail and accounts for the highest failure rate of all engine parts. As a result, its failure will have a significant negative effect on the dependability of diesel engines [1], [2]. To prevent and avert malignant turbocharger mishaps, research on turbocharger monitoring and diagnosis technology have tremendous significance and engineering application value [3], [4].

One of the commonly used techniques for conditional monitoring and fault diagnosis of rotating machinery is vibration analysis [5], [6]. Vibration signals from mechanical devices under monitoring are measured. Then, the condition identification and fault diagnosis of mechanical equipment can be accomplished by extracting their characteristics with signal analysis processing techniques [7], [8]. One way to analyze the signal is The Fourier transform. The Fourier transform can be used to evaluate and process

The associate editor coordinating the review of this manuscript and approving it for publication was Cheng Qian.

smooth signals whose frequency does not change over time strongly [9], [10]. Due to the marine turbocharger's variable operating conditions, the instantaneous frequency of its vibration signal changes swiftly. Time-varying stiffness caused by mechanical failure will also give rise to the signal's strong modulation characteristics [11]. For the above reasons, it is challenging to analyze and process the turbocharger's vibration signal using the Fourier transform [12]. The conventional approaches for processing non-stationary signals include the short-time Fourier transform (STFT) and wavelet transform. Time-frequency analysis (TFA) calculates the time-varying properties of time-series signals by extending them into time-frequency representations (TFR) [13], [14]. To improve the resolution of the time-frequency representation, obtain detailed time-varying features and maintain the reconstructability of the signal, some scholars [15], [16], [17] proposed a new time-frequency analysis method. Due to Heisenberg's inaccuracy principle, the generated time-frequency representation is commonly blurred. An accurate time-frequency description of time-varying signals is difficult to provide.

Auger and Flandrin [18], [19] developed a time-frequency rearrangement (RM) as a post-processing method for the traditional time-frequency analysis of TFA to enhance the aggregation of the original time-frequency representation. A two-dimensional redistribution integral is then performed on the time-frequency representation to obtain clearer characteristics. However, the time-frequency rearrangement is based on the time-frequency spectrum to redistribute energy from both time and frequency directions. The ability of signal reconstruction is lost. The newly assigned positions of each time-frequency point are calculated based on the time-frequency phase information. By concentrating the time-frequency energy on the instantaneous frequency estimation trajectory in the frequency direction, the synchrosqueezing transform (SST) greatly enhances the TF resolution of the traditional TFA approach [20], [21]. SST is frequently utilized in machine defect detection [22], [23], radar FM signals [24], speech processing [25], and other applications. However, the energy in the time-frequency representation still seems to be scattered. And its time-frequency aggregation is much diminished when SST is used to evaluate the turbocharger's strongly time-varying signal.

To further enhance the aggregation of the time-frequency representation when working with strongly time-varying signals, Oberlin et al. proposed a second-order and higher-order synchrosqueezing transform method [26], [27]. However, the computational capacity required to implement this method grows exponentially with the number of transform orders. Yu et al. suggested a multiple synchrosqueezing transform method [28] that effectively concentrates the time-frequency representation's energy without requiring more computation. The above Muti-order synchrosqueezing transform's time-frequency point allocation is a prevalent problem that affects all of the aforementioned methods. The time-reassigned synchrosqueezing transform, the local maximum synchrosqueezing transform (LMSST), and the synchroextracting transform were all devised by He et al. [29], [30], [31]. The LMSST successfully resolves the issue of multiple time-frequency point allocations. Its processing capacity for strongly time-varying signals increased. Whereas, the effect of the time-frequency transformation depends on whether the LMSST's window function is well-matched with the signal. The exact bandwidth of the signal components is difficult to calculate, which will also blur its time-frequency representation.

The above discussion indicates that the existing time-frequency transformation produces a blurred picture of representations, when processing strongly time-varying signals. It is difficult to capture turbocharger fault features in vibration signals. To effectively reduce the influence of the signal strongly time-varying characteristics on the time-frequency transformation, the multi-objective matched synchrosqueezing chirplet transform (MOMSSCT) method is proposed in this paper. It improves the energy concentration of the time-frequency representation for turbocharger vibration signals with strongly time-varying characteristics. On a turbocharger stand, a fault simulation test for dynamic unbalance and bearing wear was performed. Based on the results of MOMSSCT, the 1, 2 and 9-octave time domain signals of the turbocharger were reconstructed. And fault feature parameters of the turbocharger were extracted from the time domain. The turbocharger's vibration, speed, and orbit of the shaft centre were measured simultaneously at various speeds. The validity of the fault feature parameter identification is confirmed by Principal Component Analysis and Diagnostic algorithm.

This article's main contributions are summarized below.

1) This paper examines the theoretical limitations of the LMSST. It provides a detailed explanation of why LMSST cannot accurately represent the TF information of strongly time-varying signals.

2) This article presents an improved LMSST technique, MOMSSCT, which eliminates the difficulty in calculating the exact bandwidth of the signal components. It increases the energy concentration of the transformation result while maintaining signal reconstruction capability.

3) The validity of fault characteristic parameters extracted by MOMSSCT is verified by principal component analysis and diagnosis algorithm. The diagnostic accuracy rate can reach more than 85%.

4) This article gives an excellent tool for monitoring nonstationary turbocharger vibration data, which aids in determining the source of aberrant vibration.

II. METHODOLOGY

A. PROBLEM DEFINITION AND ANALYSE

The study of signal analysis is based on the SST theory. Consider a multi-component signal $s(t)$ having FM characteristics

[30], then we formulate it as:

$$s(t)=\sum_{k=1}^{K}A_k(t)e^{i\varphi_k(t)} \tag{1}$$

where K is the total number of signal components, and $A_k(t)$ and $\varphi_k(t)$ stand for the kth component's instantaneous amplitude (IA) and instantaneous phase (IP), respectively. The signal is subjected to STFT. The window function, $g(t)$, is utilized to translate it to the time-frequency domain using the transformation equation:

$$G(t,\omega)=\int_{-\infty}^{+\infty}s(u)g(u-t)e^{-i\omega(u-t)}du \tag{2}$$

When the signal is a strong time-varying signal, the phase function of the signal needs to be described by a higher-order Taylor expansion. Assuming that $\exists\varepsilon$ is sufficiently small, for $\forall t$, $\left|\varphi_k'''(t)\right| \leq \varepsilon$, and $\left|A_k'(t)\right| \leq \varepsilon$. Based on the above assumptions, the second-order expansion of the signal can be written as the form $u=t, A_k(u)=A_k(t)$. Thus $\varphi_k(u)$ and $s(u)$ can be written in the following form [30]:

$$\varphi_k(u)=\varphi_k(t)+\varphi_k'(t)(u-t)+\frac{\varphi_k''(t)(u-t)^2}{2} \tag{3}$$

$$s(u)=\sum_{k=1}^{K}A_k(t)e^{i\left[\varphi_k(t)+\varphi_k'(t)(u-t)+\frac{\varphi''(t)(u-t)^2}{2}\right]} \tag{4}$$

where $\varphi_k'(t)$ and $\varphi_k''(t)$ are the instantaneous frequency and modulation rate of the kth component of the signal. The optimal frequency interval $\Delta_\omega(t)$ in LMSST is shown in (5).

$$\Delta_\omega(t)=\sum_{k=1}^{K}\sqrt{2\left[1+\varphi_k''(t)^2\right]\ln\frac{1}{t_0}} \tag{5}$$

From(5), the $\Delta_\omega(t)$ value is calculated using the window function width t_0 and the modulation rate $\varphi_k''(t)$. However, for most signals, it is difficult to calculate the modulation rate directly. So the optimal frequency interval value is also difficult to calculate.

B. NEW MOTHED

The limitations of the LMSST method were analyzed in the previous section. For processing strongly time-varying signals, this paper proposes the MOMSSCT. Based on the Linear Chirplet Transform (LCT), a MOMSSCT is proposed. To optimize the parameters of the FM transform, the four parameters of Rayleigh entropy (RE), signal-to-noise ratio (SNR), root mean square error (RMSE) and peak signal-to-noise ratio (PSNR) are taken as targets. The optimal matching with the modulation rate of signal components is achieved. After the LCT, the LMSST is applied to the signal as a post-processing method to form a new time-frequency representation.

LCT processes the signal by adding a demodulation operator to the Fourier transform and selecting the appropriate demodulation parameter c from it for calculation. The vibration signal s is transformed to obtain the time-frequency result G. The specific calculation processes for LCT are as follows:

$$G(c,t,\omega)=\int_{-\infty}^{+\infty}s(u)g(u-t)e^{-\mathrm{i}\omega(u-t)}e^{-\mathrm{i}c(u-t)^2/2}du \tag{6}$$

$$c=\tan(\beta)\cdot\frac{F_s}{2T_s} \tag{7}$$

$$\beta=-\frac{\pi}{2}+\frac{\pi}{N_c+1},-\frac{\pi}{2}+\frac{2\pi}{N_c+1},\ldots,-\frac{\pi}{2}+\frac{N_c\pi}{N_c+1} \tag{8}$$

N_c is the number of demodulation rates, it takes the value of 11 in this mothed. The sampling time is T_s and the sampling frequency is F_s, they take the values of 1000Hz and 4s. The relationship between the rotation angle β and the demodulation rate c in the time-frequency plane is given in (7). The values of β are $-\frac{5\pi}{15}, -\frac{4\pi}{15}, -\frac{3\pi}{15}, \ldots\ldots \frac{5\pi}{15}$ respectively. The original LCT method is based on the principle of maximum time-frequency coefficient to select the appropriate demodulation parameters. But its noise immunity is poor. Redundant LCT results are generated when the noise amplitude in the signal is larger than the amplitude of the component signal.

RE, SNR, RMSE and PSNR were used as target parameters to calculate the above demodulation rate. The closer the demodulation rate and the modulation rate of the signal components are to one another and the smaller the Rayleigh entropy, the greater the time-frequency aggregation effect is. Rayleigh entropy is used to quantitatively evaluate the closeness of the demodulation rate of the windowed signal to the transform parameters. Additionally, the signal's anti-noise effect is assessed using the SNR, RMSE, and PSNR. The higher the signal-to-noise ratio, the greater the noise resistance is. The four target parameters are calculated as follows:

$$RE=-\frac{1}{2}\log_2\left(\int_{-\infty}^{\infty}\int_{-\infty}^{\infty}|G(t,w)|^{\xi}dwdt\Big/\int_{-\infty}^{\infty}\int_{-\infty}^{\infty}|G(t,w)|dwdt\right) \tag{9}$$

$$SNR=10\log_{10}\left[\left(\sum_{i=1}^{m}x(i)^2\right)\Big/\left(\sum_{i=1}^{m}(s(i)-x(i))^2\right)\right] \tag{10}$$

$$RMSE=\sqrt{\frac{1}{m}\sum_{i=1}^{m}(s(i)-x(i))^2} \tag{11}$$

$$PSNR=10\log_{10}\left[\max\left(x(i)^2\right)\Big/\frac{1}{m}\times\left(\sum_{i=1}^{m}(s(i)-x(i))^2\right)\right] \tag{12}$$

where s is the time domain signal, x is the effective signal, and m is the number of sampling points. After the above analysis, the optimal demodulation rate $\hat{c}$ can be obtained as:

$$\hat{c}(t,\omega)=\arg\min_{c}\{RE+SNR+PSNR-RMSE\} \tag{13}$$

Finally, the time-frequency transformation equation can be expressed as:

$$\begin{aligned} G_{\hat{c}}(t,\omega) &= G(\hat{c},t,\omega) \\ &= \sum_{k=1}^{K} A_k(t) e^{\mathrm{i}\varphi_k(t)} \sqrt{\frac{2\sigma\pi}{1-\mathrm{i}\sigma\left[\left(\varphi_k''(t)-\hat{c}\right)\right]}} e^{-\frac{\sigma\left[\omega-\varphi_k'(t)\right]^2}{2\left[1-\mathrm{i}\sigma\left[\left(\varphi_k''(t)-\hat{c}\right)\right]\right]}} \end{aligned} \tag{14}$$

The bandwidth Δ_ω of the multi-objective matched chirplet transform is calculated by the following equation.

$$\begin{aligned} \Delta_\omega^2 &= \frac{1}{2\pi}\int_{-\infty}^{+\infty} \omega^2 \left|G_{\hat{c}}(t,\omega)\right|^2 d\omega \\ &= \frac{1}{2\pi}\sum_{k=1}^{K}\left(A_k^2(t)\frac{2\pi}{\left(1+\left(\varphi_k''(t)-\hat{c}\right)^2\right)^{1/2}}\right) \\ &\quad \times \int_{-\infty}^{+\infty} \omega^2 e^{-\frac{\left(\omega-\varphi_k'(t)\right)^2}{\left(1+\left(\varphi_k''(t)-\hat{c}\right)^2\right)}} d\omega \\ &= \sum_{k=1}^{K} A_k^2(t)\left(\sqrt{\pi}\varphi_k'(t)+\sqrt{2}\left(1+\left(\varphi_k''(t)-\hat{c}\right)^2\right)\right) \end{aligned} \tag{15}$$

As can be seen from (15), the closer the demodulation rate and the modulation rate of the signal components, the less bandwidth is affected by the modulation rate. After the transformation, a time-frequency rearrangement is performed by the LMSST method. The LMSST is applied as a post-processing method. And a local maximum compression is applied to the signal to form a new time-frequency representation (TFR) $MG_{\hat{c}}^{s}(t,\xi)$. The specific steps of the LMSST method are as follows:

$$MG_{\hat{c}}^{s}(t,\xi) = \int_{-\infty}^{+\infty} G_{\hat{c}}(t,\omega)\delta(\xi-\hat{\omega}(t,\omega))d\omega \tag{16}$$

where the instantaneous frequency estimate is calculated from (17):

$$\hat{\omega}(t,\omega) = \begin{cases} \underset{\omega}{\arg\max}\left|G_{\hat{c}}(t,\omega)\right|, & \omega \in [\omega-\Delta,\omega+\Delta], \\ if\ \left|G_{\hat{c}}(t,\omega)\right| \neq 0 & \\ 0, & \text{if } \left|G_{\hat{c}}(t,\omega)\right| = 0 \end{cases} \tag{17}$$

Equation (17) produces an unbiased estimate of the instantaneous frequency when the SST's bandwidth matches that of the signal component time-frequency transform. Algorithm 1 is the implementation code of MOMSSCT.

Algorithm 1 MOMSSCT

```
Step 1: Initialization
Input s, $T_s$ and $F_s$ in Equation (7)~(12).
Step 2: Improved linear chirplet transform
Calculate RE, SNR, RMSE and PSNR by Equation (9)~(12).
Calculate optimal demodulation rate $\hat{c}$ by Equation (13).
Obtain $G_{\hat{c}}(t,\omega)$ through performing LCT by Equation (6).
Step 3: Time-frequency post-processing
Calculate$\Delta_\omega$ by Equation (15).
Perform LMSST by Equation (16) and (17).
```

III. EXPERIMENT

A. SIMULATION TEST

The effectiveness of the time-frequency analysis of MOMSSCT is verified with a set of simulated strong time-varying signals, which consist of two components. The two components have nonlinear characteristics. And the latter has stronger time-varying characteristics. This signal is designed in such a way to test the ability of the MOMSSCT to handle strongly time-varying signals.

$$\begin{aligned} s(t) &= sin(2\pi\,(15t+4sin2t)) \\ &\quad + sin(2\pi(35t+arctan(2(t-1)^2))) \end{aligned} \tag{18}$$

With a sampling frequency of 1000Hz and a sampling duration of 4s, the simulated signal is produced. Meanwhile, we added Gaussian white noise with a signal-to-noise ratio of 3db to the signal. The signals produced using these parameters meet the criteria for the signal processing method test. Figure 1 compares the outcomes of various time-frequency transform techniques. The time-frequency diagram of the short-time Fourier transform is shown in Figure 1(a). Because of the Heisenberg inaccuracy principle's restriction and the strong time-varying properties of the signal, the time-frequency results are not aggregated and there is severe energy blurring. A continuous wavelet transform time-frequency diagram is shown in Figure 1(b). Only the general shape of the signal's components can be seen because of the signal's strong time-varying properties. The Fourier synchrosqueezing transform time-frequency diagram in Figure 1(c) shows the two signal components' time-frequency trajectories, though their energies are still a little hazy. The time-frequency energy aggregation of the wavelet synchrosqueezing transform time-frequency map is shown in Figure 1(d). The time-frequency diagram for the local maximum synchrosqueezing transform is shown in Figure 1(e). There is still some energy diffusion in the high-frequency component despite the relatively effective time-frequency energy aggregation and improved frequency trajectory estimation. Figure 1(f) is the time-frequency diagram of the MOMSSCT proposed in this paper. Its energy is highly concentrated. The LMSST's average spread widths of high and low frequencies in 4 seconds are 1.9 Hz and 2.1 Hz,

TABLE 1. Test instruments and equipment in stand test.

Equipment name	Model	Range	Precision
Vibration test system	LMS SCADAS Mobile	—	—
Turbocharger measurement and control system	NI	—	—
Acceleration sensor	B&K 4534-B	±700g	—
Temperature sensors	K index thermocouple	0~1000°C	±2%
Rotational speed sensor	EM3309	—	±0.5%
Orbit of the shaft centre Eddy current sensor	Bently3300	10~100mils	—
Pressure sensors	Y-153BF	0~1.6MPa	±0.4%

respectively. While the average spread widths of high and low frequencies in 4 seconds are 1.2 Hz and 1.3 Hz for the MOMSSCT. The frequency spread width reduces by 37.5%. So this method can effectively analyze the characteristics of strong time-varying signals.

B. PRACTICAL TEST SETTING

A type of turbocharger with a pressure ratio of 4.5, which can be matched with a marine diesel engine with a power range of 600 kW to 1000 kW, is used in the test. The fault simulation tests of dynamic imbalance and bearing wear were carried out in the turbocharger stand to provide fault samples for the subsequent verification of the feature parameter extraction method.

Figure 2 shows the schematic diagram of the test system, in which T, P and ω represent temperature, pressure and speed sensors [32]. V and O represent the vibration and orbit of shaft centre sensors. The test stand primarily consists of a turbocharger, a combustion chamber, and a gas valve. The injector injects fuel into the combustion chamber for combustion. The high-temperature gas enters the turbine to do work to drive the rotor shaft rotation. The coaxial compressor compresses the air. Finally, when the self-circulation valve opens, the pressurized air enters the combustion chamber to form a self-circulation. Figure 3 (a) shows the site of the turbocharger test stand. In Figure 3 (b) and (c), 1∼8 are vibration sensors, 9 are speed sensors, and 10 are displacement sensors for measuring the shaft orbit. The vibration sensors operate in the temperature range of -55 to +125 °C. The turbocharger case temperature exceeds this range. So the vibration sensors are mounted on the turbocharger base to avoid damage.

The temperature and pressure of the turbine and compressor before and after intake/ outlet, the speed of the turbocharger, the vibration acceleration of the turbocharger base and the orbit of the shaft centre were measured in the test. The vibration, orbit of the shaft centre and speed were collected by the Siemens LMS SCADAS Mobile system. The speed signal, temperature and pressure signals were collected by the turbocharger measurement and control platform of the experimental site. The main test instruments and equipment used in the test are shown in Table 1.

TABLE 2. Turbocharger failure test program table.

Turbocharger status	Condition characterization parameters	Unit	Remarks
Dynamic unbalance condition	Rotor dynamic unbalance & Bearing surface roughness Ra value	mg·mm & µm	1)10.0 mg·mm 0.5µm 2)7.6 mg·mm 0.5µm
Dynamic unbalance & bearing wear condition	Rotor dynamic unbalance & Bearing surface roughness Ra value	mg·mm & µm	1)10.0 mg·mm 1.2µm
Normal status	Rotor dynamic unbalance & Bearing surface roughness Ra value	mg·mm, µm	1)3.1 mg·mm 0.5µm

The turbocharger was put through four different testing sequences: severe dynamic imbalance, severe dynamic imbalance plus bearing wear, slight dynamic imbalance and normal condition. To reduce the test cost, the severe dynamic imbalance failure test was first carried out; secondly, the faulty bearing was replaced for the double failure test of severe dynamic imbalance plus bearing wear; then the normal bearing was replaced and the rotor dynamic imbalance was reduced on the dynamic balancing machine for the minor dynamic imbalance failure test; finally, the dynamic imbalance of the rotor was reduced to the normal value on the dynamic balancing machine for the normal state test. The turbocharger test speed in working condition is from 35000 r/min to 60000 r/min, the interval is 2500 r/min, and the test program is shown in Table 2. There are two sets of experiments in the dynamic unbalance condition. There is one set of experiments for each of the other states. In the subsequent subsections, we processed and analyzed the test data using MOMSSCT.

C. TEST DATA PROCESS AND EVALUATION MATRIX

One of the frequent failures of turbochargers is rotor imbalance. According to statistics, rotor imbalance is a factor in more than 50% of failures of rotating machinery. The following aspects need to be taken into account while analyzing the mechanism of marine diesel engine turbocharger imbalance failure. When a turbocharger turns at a speed of up to tens of thousands of revolutions per minute, the unbalanced mass of the rotor—however small—will result in a very strong centrifugal force. A turbocharger's rotor rotates once to produce one shock when there is an unbalance. And its vibration response characteristics are mirrored in 1× frequency peak. If the compressor impeller has n main blades and n from blades. Then the rotor rotates 1 turn and the impeller blade air oscillates n times, producing n times of vibration response characteristics. This paper will focus on the 9× frequency of the vibration signal, because the compressor impeller has 9 main blades and 9 from blades.

One of the most common causes of component failure is wear. It occurs when two objects come into touch with one another and the surface micro-convex peaks continue to fall off. It eventually damages the material's surface or causes residual deformation. There isn't a lot of research on turbocharger bearing wear failure right now. The load, friction coefficient, eccentricity, oil film pressure, temperature and bearing capacity of the sliding bearing all attain a condition of dynamic equilibrium when it operates in the state of hydrodynamic lubrication. When the bearing area wears out and fails, there will be a local pressure surge that will hit the shaft tile's surface and cause excitation. At the same time, the oil film thickness changes, making the turbocharger vibration

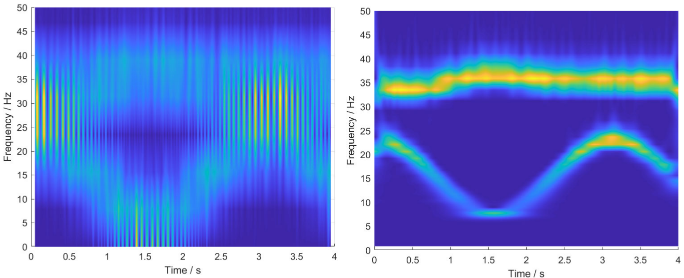

(a)STFT time-frequency diagram (b)CWT time-frequency diagram

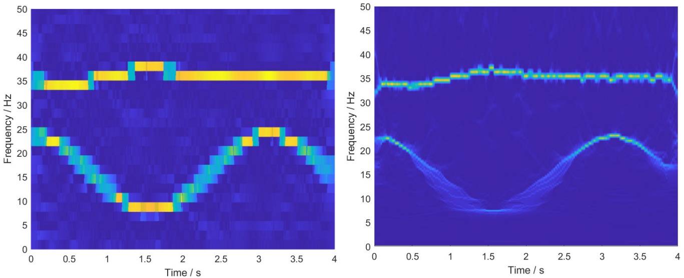

(c)FSST time-frequency diagram (d)WSST time-frequency diagram

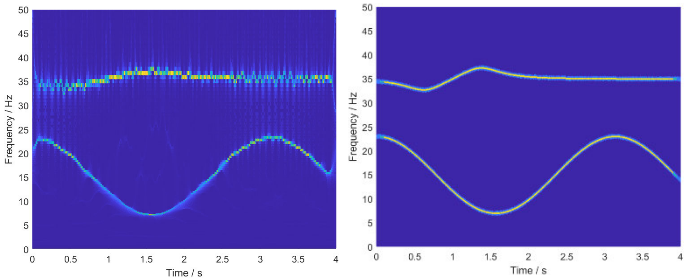

(e)LMSST time-frequency diagram (f)MOMSSCT time-frequency

FIGURE 1. **Comparison of the effect of different time-frequency transformation methods.**

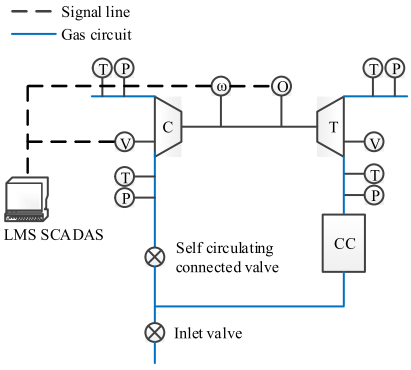

FIGURE 2. **Schematic diagram of the turbocharger test system.**

response also change. According to the preliminary analysis of the vibration response signal spectrum, 2× frequency and the blade through frequency of turbocharger is more sensitive to bearing wear failure.

Figures 4 and 5 depict the turbocharger's vibration signals at 60,000 r/min and 50,000 r/min under normal, dynamic unbalance and dynamic unbalance with bearing wear situations. Under turbocharger speeds of 60,000 r/min and 50,000 r/min, when the turbocharger switches from normal to dynamic unbalance, the root mean square value and variance of the signal increase. And the changing of the maximum and minimum values of the signal is not apparent. When the turbocharger switches from dynamic unbalance to double fault, the root mean square value and variance of the signal decrease, and the maximum and minimum values of the signal are changed.

Figure 6 and Figure 7 are the time-frequency diagrams obtained by the MOMSSCT method under the three fault states of the turbocharger in 60,000 r/min and 50,000 r/min operating conditions. It can be seen that the time-frequency energy is concentrated. Figure 6 shows the results of the time-frequency transformation of the turbocharger at 60,000 r/min. The fundamental frequency is $60{,}000 \div 60 = 1000$ Hz. It is shown in Figure 6(a) as the horizontal line at 1000 Hz in the vertical coordinate. And similarly its 2×, 3× and 9× frequencies are the horizontal lines at 2000 Hz, 3000 Hz and 9000 Hz in the vertical coordinate. Figure 7 shows the turbocharger at 50,000 r/min, and its 1×, 2×, 3× and 9× frequencies are the horizontal lines at 833 Hz, 1667 Hz, 2500 Hz and 7500 Hz. In the 60,000 and 50,000 r/min speed conditions, when comparing Figure (a) and Figure (b), the turbocharger changes from normal to dynamic unbalance. The 1× frequency amplitude increases and the 9×

(a) Turbocharger test stand

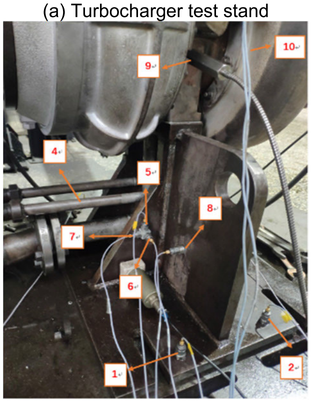

(b) Sensor arrangement diagram

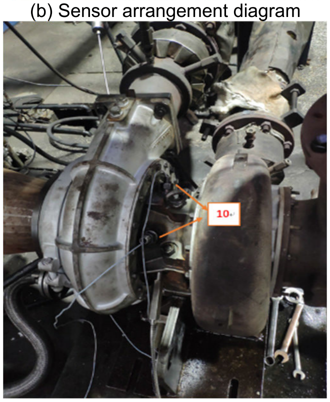

(c) Sensor arrangement diagram

FIGURE 3. Turbocharger test stand.

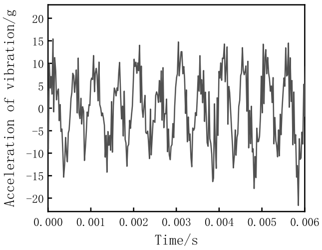

(a) Normal condition

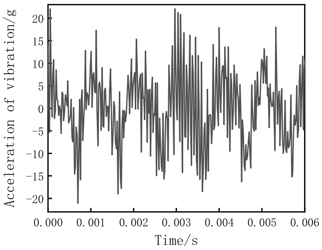

(b) Dynamic imbalance

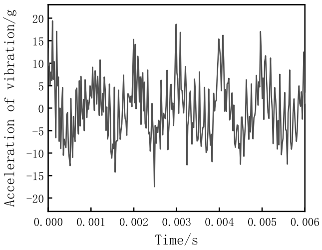

(c) Dynamic imbalance plus bearing wear

FIGURE 4. Vibration signal of turbocharger 60,000 r/min operation.

frequency amplitude decreases. When comparing Figure (b) and Figure (c), the turbocharger changes from dynamic unbalance to double fault, and the 2× frequency and 9× frequency amplitude increase.

From the obtained time-frequency results, the 1×, 2×, and 9× domain vibration signals are reconstructed. And the frequency lines of 1×, 2×, and 9× are extracted along the frequency ridges. Their time domain signal are reconstructed according to Equation (19):

$$s(t) = \frac{1}{2\pi \hat{g}(0)} \int_{-\infty}^{+\infty} \int_{-\infty}^{+\infty} MG_{\hat{c}}^{s}(u, \xi) e^{i\omega t} du d\xi \tag{19}$$

where $\hat{g}(\omega)$ is the Fourier transform of the window function.

Figure 8 and Figure 9 show the time-domain vibration signals of 1× frequency, 2× frequency, and 9× frequency after the reconstruction of time-frequency maps. It can be seen that the instantaneous frequency estimation accuracy based on the MOMSSCT method is high. It makes the reconstruction accuracy of each component of the vibration signal also relatively good. And the noise in the signal is small. When the turbocharger is in three different states, the parameters such as amplitude and energy of its 1× frequency, 2× frequency and 9× frequency vibration signals change. In the turbocharger 60,000 r/min and 50,000 r/min conditions, when it changes from the normal state to the dynamic unbalance state, the amplitude of its 1× frequency vibration signal rises and the amplitude of 9× frequency decreases. When the turbocharger changes from the dynamic unbalance state to the double fault, the amplitude of its 2× frequency and 9× frequency vibration signal rises.

According to the aforementioned fault cause analysis, 1× frequency, 2× frequency and 9× frequency are more sensitive to the two faults of dynamic unbalance and bearing wear. According to the reconstructed 1, 2 and 9-octave component signals, the fault characteristic parameters such as the effective value of vibration (R_1, R_2, R_9), the ratio between octave components (E_{21}, E_{91}, E_{92}) and the ratio of the effective value of vibration to health status (RN_1, RN_2, RN_9) can be extracted. The variation coefficients of parameters also contain certain fault information. And the fault characteristic parameters are also extracted, such as the rotor frequency phase

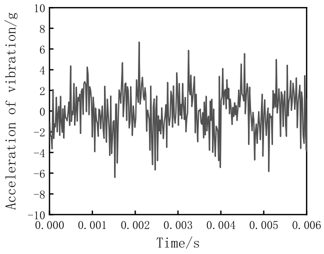

(a) Normal condition

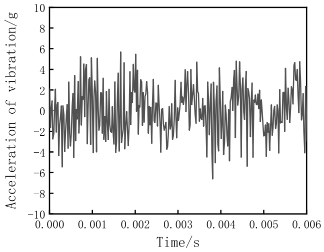

(b) Dynamic imbalance

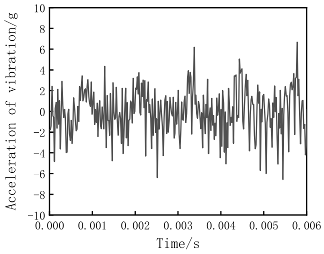

(c) Dynamic imbalance plus bearing wear

FIGURE 5. **Vibration signal of turbocharger 50,000 r/min operation.**

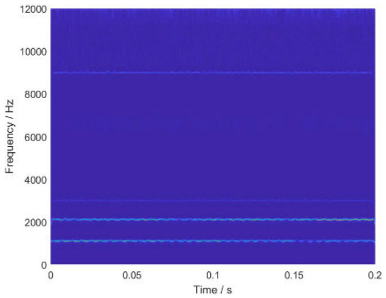

(a) Normal condition

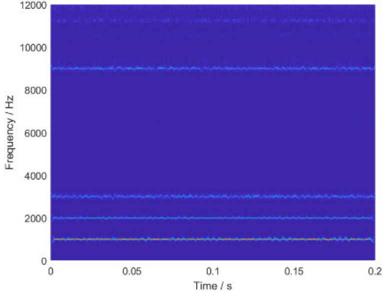

(b) Dynamic imbalance

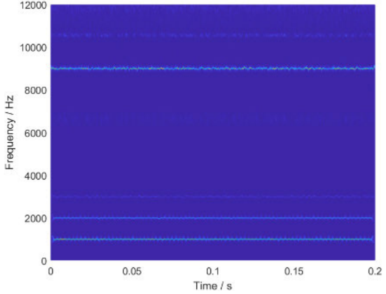

(c) Dynamic imbalance plus bearing wear

FIGURE 6. **Turbocharger 60,000 r/min operating conditions MOMSSCT transformation time and frequency diagram.**

difference variation coefficient, the variation coefficient of the effective value of the frequency vibration, the standard deviation of the effective value of the frequency vibration, the variation coefficient of the instantaneous frequency of the frequency vibration, the speed fluctuation coefficient of the turbocharger, and the variation coefficient of the cross and longitudinal coordinates of the rotor axis orbit. Because R_1 and R_2 will increase with the rise of rotational speed, the two parameters $R_1 \big/ f_N^2$ and $R_2 \big/ (2f_N)^2$ are extracted and named as rotor unbalance factor and bearing wear factor. The summary of 18 parameters is detailed in Table 3.

D. PRACTICAL TEST RESULT

Table 4 shows the turbocharger vibration data under the four states of the turbocharger. after MOMSSCT and signal reconstruction, the extracted turbocharger fault characteristic parameters can provide data support for the subsequent characteristic parameter merit selection.

Figure 10 shows the variation law of the characteristic parameters with the degree of failure. The variation of the RMS value of the turbocharger, the RMS value of the 2× frequency vibration, the RMS value of the 9× frequency vibration, and the standard deviation of the RMS value of the 1× frequency vibration with the dynamic unevenness of the rotor are shown in Figure 10(a). The RMS value of the 1× frequency vibration and the standard deviation of the RMS value of the frequency vibration increase with the increase of the dynamic unevenness. The RMS value of the 2× frequency vibration and the RMS value of the 9× frequency vibration decrease with the increase of the dynamic unevenness. The changes of the turbocharger 1× frequency vibration RMS, 2× frequency vibration RMS, 9× frequency vibration RMS, and the standard deviation of the 1x frequency vibration RMS with the roughness of the bearing are shown in Figure 10(b). The 1× frequency vibration RMS and the 1× frequency vibration RMS decrease with the increase of the bearing surface roughness. The 2× frequency vibration RMS and 9× frequency vibration RMS increase with the increase of the bearing surface roughness.

E. COMPARISON OF VISUALIZATION RESULTS

The validity of the characteristic parameters was verified using sample data of the turbocharger. The states when the data is collected include a health condition, a minor dynamic unbalance failure, a severe dynamic unbalance failure, and a dynamic unbalance plus bearing wear failure. The sample data contains the vibration acceleration signals, rotor speed

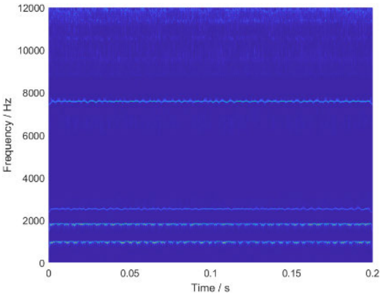

(a) Normal condition

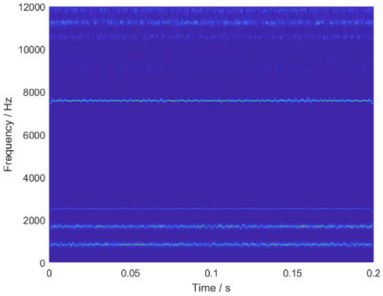

(b) Dynamic imbalance

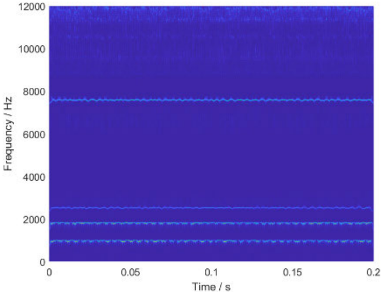

(c) Dynamic imbalance plus bearing wear

FIGURE 7. **Turbocharger 50,000 r/min operating conditions MOMSSCT transformation time and frequency diagram.**

signals and shaft centre orbit of the measurement points. And the operating points of the turbocharger at different health states and speeds are given in Table 5.

Table 6 shows the data classification and labelling of each fault state of the turbocharger. A, B, C and D represent the healthy state, minor dynamic unbalance fault, severe dynamic unbalance fault and dynamic unbalance plus bearing wear fault, respectively. The fault data set of the turbocharger was divided into A1∼A3, B1∼B3, C1∼C3 and D1∼D3. The classification effect of the feature parameter extraction method of different fault samples was visually determined. The combination of different working condition samples under each fault will be processed concerning the four-factor three-level orthogonal test (Table 7). And the combinations were S1 (A1/B1/C1/D3), S2 (A1/B2/C3/D2), S3 (A1/B3/C2/D3), S4 (A2/B1/C3/D3), S5 (A2/B2/C2/D1), S6 (A2/B3/C1/D2), S7 (A3/B1/C2/D2), S8 (A3/B2/C1/D3), S9 (A3/B3/C3/D1). S1∼S9 denote 9 generalized working conditions. It can be seen that 4 health states are included in each generalized working condition.

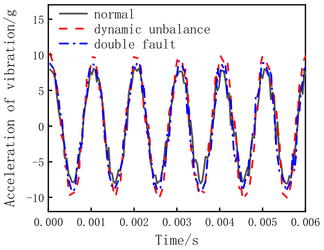

(a)1× frequency

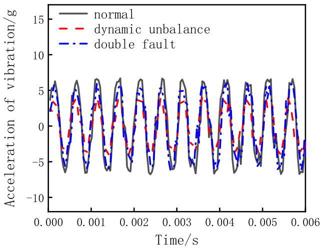

(b)2× frequency

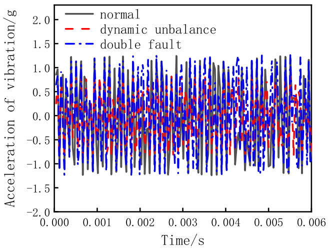

(c)9× frequency

FIGURE 8. **Comparison of reconstructed signals in three states of turbocharger 60,000 r/min operating conditions.**

TABLE 3. **Table of fault characteristic parameters.**

No.	Statistical Characteristics	No.	Statistical Characteristics
1	RMS value of rotor frequency vibration	10	Coefficient of variation of the phase difference of rotor working frequency
2	RMS value of rotor 2× frequency vibration	11	Coefficient of variation of the RMS value of the 1× frequency vibration
3	RMS value of rotor 9× frequency vibration	12	The standard deviation of the RMS value of the 1× frequency vibration
4	Rotor 2× frequency to frequency vibration energy ratio	13	Coefficient of variation of instantaneous frequency of 1× frequency vibration
5	Rotor 9× frequency to frequency vibration energy ratio	14	Coefficient of variation of turbocharger speed
6	Rotor 9× frequency to 2× frequency vibration energy ratio	15	Coefficient of variation of rotor transverse shaft centre orbit
7	The ratio of RMS value of 1×-frequency vibration to that of the healthy state	16	Coefficient of variation of rotor longitudinal shaft centre orbit
8	The ratio of RMS value of 2×-frequency vibration to that of the healthy state	17	Rotor unbalance factor
9	The ratio of RMS value of 9×-frequency vibration to that of the healthy state	18	Bearing wear factor

To confirm the ability of the extracted feature parameters to characterize the fault features, the data were mapped from the original space to the two-dimensional space for visualization

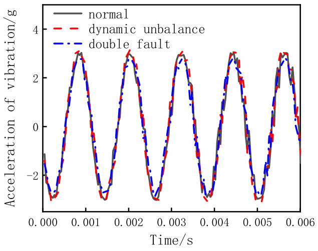

(a)1× frequency

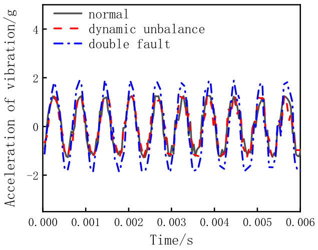

(b)2× frequency

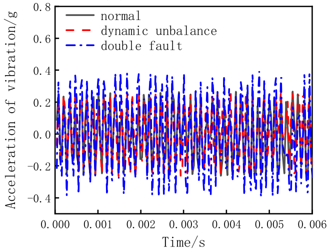

(c)9× frequency

FIGURE 9. **Comparison of reconstructed signals in three states of turbocharger 50,000 r/min operating conditions.**

TABLE 4. **Extracted turbocharger characteristic parameters for each state.**

No./ unit	1/(m/s^2)	2/(m/s^2)	3/(m/s^2)	4/dimensionless	5/dimensionless	6/dimensionless	7/dimensionless	8/dimensionless	9/dimensionless
Normal	5.68	4.78	0.88	0.84	0.15	0.18	1.02	1.01	1.01
Dynamic unbalance light	6.38	2.84	0.72	0.44	0.11	0.25	1.14	0.60	0.74
Dynamic unbalance heavy	7.09	2.79	0.60	0.39	0.08	0.22	1.27	0.59	0.56
Double fault	6.75	4.22	0.86	0.63	0.13	0.20	1.21	0.90	0.84
No./ unit	**10/dimensionless**	**11/dimensionless**	**12/(m/s^2)**	**13/dimensionless**	**14/dimensionless**	**15/dimensionless**	**16/dimensionless**	**17/(m)**	**18/dimensionless**
Normal	-2.27	5.86E-02	0.33	-2.67	1.32	1.52	-2.12	5.68E-06	1.19E-06
Dynamic unbalance light	-2.70	6.34E-02	0.36	-3.10	0.43	1.02	-0.75	6.38E-06	7.10E-07
Dynamic unbalance heavy	-2.45	7.14E-02	0.41	-2.47	-0.45	0.97	0.52	7.09E-06	6.96E-07
Double fault	-2.09	7.09E-02	0.40	-2.02	-2.81	-1.39	2.88	6.75E-06	1.06E-06

TABLE 5. **Turbocharger failure simulation test conditions.**

Fault Type	Turbocharger speed(r/min)
Health Status	40000/50000/60000
Rotor unbalance slight	40000/50000/60000
Rotor unbalance severe	40000/50000/60000
Rotor unbalance severe & bearing wear	40000/50000/60000

using Principal Component Analysis (PCA) [33]. The steps of the principal component analysis method are as follows:

1. De-mean normalize the matrix X_o composed of the original data to obtain $X = (x_i^k)_{r*p}$.

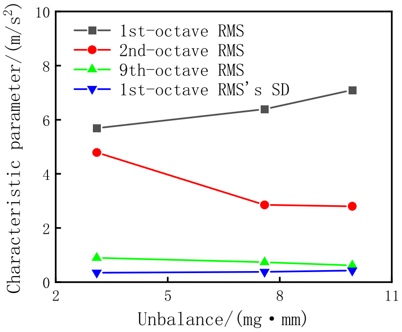

(a)Dynamic imbalance

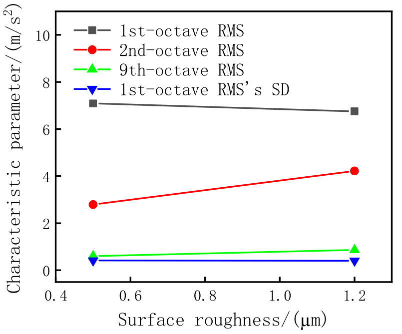

(b)Bearing wear

FIGURE 10. **Variation law of characteristic parameters with the degree of failure.**

TABLE 6. **Turbocharger fault data classification table.**

Group	Fault Type	Turbocharger speed(r/min)
A1	Health Status	40000
A2		50000
A3		60000
B1	Rotor unbalance slight	40000
B2		50000
B3		60000
C1	Rotor unbalance severe	40000
C2		50000
C3		60000
D1	Rotor unbalance severe & bearing wear	40000
D2		50000
D3		60000

2. Calculate the correlation coefficient matrix C.

$$C = (s_{ij})_{p*p} \tag{20}$$

$$s_{ij} = \frac{1}{r-1}\sum_{k=1}^{r}(x_i^k - \overline{x_i})(x_j^k - \overline{x_j})i, j = 1, 2, \cdots, p \tag{21}$$

where r is the number of samples, p is the number of feature parameters. And $\overline{x_i}$ is the average of the i-th feature parameter in matrix X.

3. Calculate the eigenvalues λ_i and eigenvectors a_i of the correlation coefficient matrix, $i = 1, 2, \ldots, p$;

TABLE 7. **Four-factor three-level orthogonal test table.**

No.	Factor1	Factor2	Factor3	Factor4
1	1	1	1	1
2	1	2	3	2
3	1	3	2	3
4	2	1	3	3
5	2	2	2	1
6	2	3	1	2
7	3	1	2	2
8	3	2	1	3
9	3	3	3	1

TABLE 8. **The common characteristics parameters for turbocharger fault diagnosis.**

No.	Characteristics	No.	Characteristics
1	Mean Value	10	Effective value
2	Root mean square value	11	Waveform factor
3	Variance	12	Time-frequency energy entropy
4	Peak value	13	Average frequency
5	Peak-to-peak value	14	Frequency centre
6	kurtosis	15	0~3kHz spectrum energy
7	skew	16	3~6kHz spectrum energy
8	Square root amplitude	17	6~9kHz spectrum energy
9	Absolute mean	18	9~12kHz spectrum energy

4. Transform X to get the new feature matrix F_i after dimensionality reduction;

$$F_i = a_i^T Xi = 1, 2, \ldots, d; \tag{22}$$

where d is the dimensionality of the data after dimensionality reduction. It is taken as 2 in this paper.

Common feature parameters for turbocharger fault diagnosis were selected for comparison with those extracted by MOMSSCT. The G2 and G3 data were randomly selected for analysis. The common feature parameters for turbocharger fault diagnosis are shown in Table 8. The common fault characteristic parameters of turbochargers were extracted from G2 and G3 according to the table. Then it was visualized using the PCA. Their PCA extraction visualization results are shown in Figures 11(a) and (b). The aggregation degree of the same fault type in two-dimensional space in G3 data is acceptable. But the distribution of normal state samples in two-dimensional space in G2 data is not aggregated enough. And the splitting is serious. It indicates that after the PCA extraction of common features, the aggregation of samples of the same fault type is not high enough. In Figure 11 (a) and (b), the rotor imbalance case is close to the double faults. And even some data overlap together. Their sample features are less distinguished. The results indicate that the common features of turbochargers shown in Table 8 are difficult to achieve an effective classification of the fault states of turbochargers.

TABLE 9. **Source domain auxiliary data and target domain data set division.**

Data category	Work condition	Fault category and severity	Quantity
Source domain auxiliary data (simulation)	35000、40000、50000、60000r/min	Normal	180
		Slight/ moderately /severe dynamic unbalance	720
		Slight/ moderately /severe bearing wear	720
		Dynamic unbalance combined with bearing wear	720
Target domain data (measured)	35000、40000、50000、60000r/min	Normal	40
		Slight/ moderately /severe dynamic unbalance	120
		Slight/ moderately /severe bearing wear	120
		Dynamic unbalance combined with bearing wear	120

For S2 and S6 data, the turbocharger data were processed by MOMSSCT. Then the signal was reconstructed. And the fault feature parameters were extracted. The visualization results of the feature parameters calculated by the PCA method are shown in Figure 11(c) and (d). The interval between different kinds of fault samples is large and the distinction is obvious. The same fault types are clustered together without the situation that different fault types cross each other. This indicates that the extracted feature parameters effectively reflect the fault characteristics of the turbocharger. It achieved an effective classification of the four states. In addition, it can be seen from Figure 11(c) and (d) that the extracted feature parameters are unaffected by the changes in the operating conditions of the turbocharger. Under different generalized operating conditions, the feature parameter construction method proposed in this paper can obtain a feature matrix with excellent performance. It effectively solves the problem of classification performance degradation of the turbocharger due to changes in operating conditions.

To verify the effectiveness of the MOMSSCT extracted features, the TrAdaBoost transfer learning algorithm is used to diagnose the feature data. The characteristic data of three faults simulated under 35000, 40000, 50000 and 60000 r/min operating conditions of the turbocharger were used as the source domain auxiliary data. The actually measured fault characteristic data of the turbocharger were used as the target domain data. Each fault was divided into three different fault degrees. The data set was divided into a training set and a test set according to a certain ratio, as shown in Table 9 and Tab. 10. The total number of sample data for simulation is 2840.

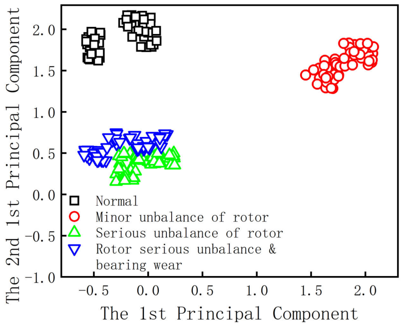

(a) Common feature parameters for G2 data

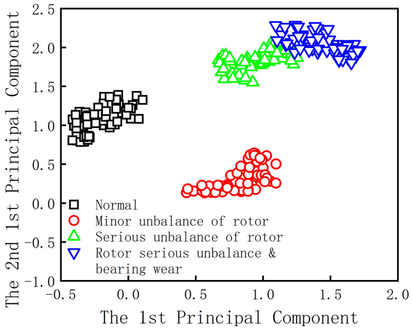

(b) Common feature parameters for G6 data

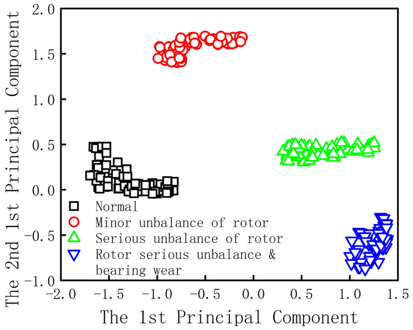

(c) MOMSSCT feature parameters for G2 data

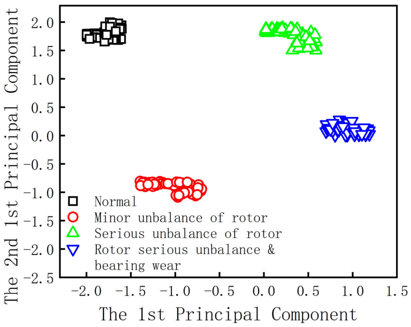

(d) MOMSSCT feature parameters for G6 data

FIGURE 11. **PCA visualization results of turbocharger characteristic parameters.**

TABLE 10. **Training set and test set samples.**

Data category	Data content	Data quantity
Training set	Source domain auxiliary data	2400
	A small amount of target domain data1	20
	A small amount of target domain data 2	40
Test set	Target domain data	400

TABLE 11. **Accuracy of the algorithm with different numbers of target samples in the training set.**

Transfer work condition	Number of target samples in training set	TrAdaBoost algorithm accuracy
Source Domain → Target Domain	20	0.89
	40	0.96

The number of source domain auxiliary training samples is 2400 (4 loads, 10 fault states, 60 samples for each state). The number of target domain data in the training set is 20 and 40, respectively. And the number of target domain samples is 400 (4 loads, 10 fault states, 10 samples for each state).

As shown in Table 10, the training set contains a small amount of target domain data, whose numbers are 20 and 40, respectively. The test set contains a large amount of target domain data with untagged state labels, the number of which is 400. The data in the test set are the actual measured turbocharger data on the test stand. And the data in the training set are the data simulated using the turbocharger model plus very few actual measured data. If the diagnosis success rate is high, it indicates that MOMSSCT is effective.

Table 11 shows the accuracy of the algorithm with different numbers of target samples in the training set. The accuracy of the algorithm increases when the number of target samples in the training set increases. The accuracy of the TrAdaBoost algorithm reaches more than 85% in both cases. The algorithm changes the weights of each target sample in the training set through the training of source domain auxiliary data. It enables the fault diagnosis model to better diagnose the target domain data (Measured turbocharger data) and improve the overall recognition effect of the model on the target domain data. The diagnostic accuracy indicates that the fault features extracted by MOMSSCT can effectively diagnose turbocharger faults.

IV. CONCLUSION

(1) For the turbocharger vibration signal with strong time-varying characteristics, a MOMSSCT method can effectively avoid the fuzzy time-frequency transformation results. The proposed method has high time-frequency energy aggregation and clear trajectories. The frequency spread width is reduced by 37.5% compared with the existing methods. It can effectively analyze the strong time-varying signal of turbocharger.

(2) The fault feature parameters were extracted based on MOMSSCT. The RMS value of the 1× frequency vibration and the standard deviation of the RMS value of the frequency vibration increase with the increase of the dynamic unevenness. The RMS value of the 2× frequency vibration and the

RMS value of the 9× frequency vibration decrease with the increase of the dynamic unevenness.

(3) The proposed feature construction method has a better ability to classify faults than the common methods. The visualization results showed that the distinction between different kinds of faults was obvious. The selected feature parameters had good fault classification ability at different speeds of the turbocharger. Using the fault features extracted by MOMSSCT, the diagnostic accuracy rate can reach more than 85%.

REFERENCES

[1] X. Cui, C. Yang, J. R. Serrano, and M. Shi, "A performance degradation evaluation method for a turbocharger in a diesel engine," *Roy. Soc. Open Sci.*, vol. 5, no. 11, Nov. 2018, Art. no. 181093.

[2] M. Yucesan, V. Başhan, H. Demirel, and M. Gul, "An interval type-2 fuzzy enhanced best-worst method for the evaluation of ship diesel generator failures," *Eng. Failure Anal.*, vol. 138, Aug. 2022, Art. no. 106428.

[3] D. Han, C. Bi, and J. Yang, "Nonlinear dynamic behavior research on high-speed turbo-expander refrigerator rotor," *Eng. Failure Anal.*, vol. 96, pp. 484–495, Feb. 2019.

[4] B. Li, Y. Cui, S. Liu, Y. Liu, X. Wang, and Z. Ding, "Experimental and numerical study based on ductile failure for the tri-hub burst of turbocharger turbine," *Eng. Failure Anal.*, vol. 138, Aug. 2022, Art. no. 106295.

[5] G. Manhertz and A. Bereczky, "STFT spectrogram based hybrid evaluation method for rotating machine transient vibration analysis," *Mech. Syst. Signal Process.*, vol. 154, Jun. 2021, Art. no. 107583.

[6] C. Malla and I. Panigrahi, "Review of condition monitoring of rolling element bearing using vibration analysis and other techniques," *J. Vibrat. Eng. Technol.*, vol. 7, no. 4, pp. 407–414, Aug. 2019.

[7] Y. Zhang, L. Duan, and M. Duan, "A new feature extraction approach using improved symbolic aggregate approximation for machinery intelligent diagnosis," *Measurement*, vol. 133, pp. 468–478, Feb. 2019.

[8] M. Hosseinpour-Zarnaq, M. Omid, and E. Biabani-Aghdam, "Fault diagnosis of tractor auxiliary gearbox using vibration analysis and random forest classifier," *Inf. Process. Agricult.*, vol. 9, no. 1, pp. 60–67, Mar. 2022.

[9] G. Yu, T. Lin, Z. Wang, and Y. Li, "Time-reassigned multisynchrosqueezing transform for bearing fault diagnosis of rotating machinery," *IEEE Trans. Ind. Electron.*, vol. 68, no. 2, pp. 1486–1496, Feb. 2021.

[10] M. Jalayer, C. Orsenigo, and C. Vercellis, "Fault detection and diagnosis for rotating machinery: A model based on convolutional LSTM, fast Fourier and continuous wavelet transforms," *Comput. Ind.*, vol. 125, Feb. 2021, Art. no. 103378.

[11] S. Wang, X. Chen, G. Li, X. Li, and Z. He, "Matching demodulation transform with application to feature extraction of rotor rub-impact fault," *IEEE Trans. Instrum. Meas.*, vol. 63, no. 5, pp. 1372–1383, May 2014.

[12] V. Sharma and A. Parey, "Extraction of weak fault transients using variational mode decomposition for fault diagnosis of gearbox under varying speed," *Eng. Failure Anal.*, vol. 107, Jan. 2020, Art. no. 104204.

[13] A. Ketata, I. Ketata, and Z. Driss, "A DFT spectrum acoustic analysis for investigating pulse duration effect on performance, psychoacoustic sound level of turbocharger turbines through C++ FDM code," *Arabian J. Sci. Eng.*, vol. 47, no. 7, pp. 8945–8968, Jul. 2022.

[14] A. Moshrefi and M. Shalchian, "Improved knock detection method based on new time-frequency analysis in spark ignition turbocharged engine," *Automot. Sci. Eng.*, vol. 8, no. 3, pp. 2759–2768, 2018.

[15] B. Boashash and S. Ouelha, "Designing high-resolution time-frequency and time-scale distributions for the analysis and classification of non-stationary signals: A tutorial review with a comparison of features performance," *Digit. Signal Process.*, vol. 77, pp. 120–152, Jun. 2018.

[16] Z. Feng and X. Chen, "Adaptive iterative generalized demodulation for nonstationary complex signal analysis: Principle and application in rotating machinery fault diagnosis," *Mech. Syst. Signal Process.*, vol. 110, pp. 1–27, Sep. 2018.

[17] Q. Liu, Y. Wang, and Y. Xu, "Synchrosqueezing extracting transform and its application in bearing fault diagnosis under non-stationary conditions," *Measurement*, vol. 173, Mar. 2021, Art. no. 108569.

[18] F. Auger and P. Flandrin, "Improving the readability of time-frequency and time-scale representations by the reassignment method," *IEEE Trans. Signal Process.*, vol. 43, no. 5, pp. 1068–1089, May 1995.

[19] Z. Hua, J. Shi, X. Jiang, Y. Luo, and Z. Zhu, "Matching and reassignment based time-frequency enhancement for rotating machinery fault diagnosis under nonstationary speed operations," *Meas. Sci. Technol.*, vol. 32, no. 8, Aug. 2021, Art. no. 084002.

[20] I. Daubechies, J. Lu, and H.-T. Wu, "Synchrosqueezed wavelet transforms: An empirical mode decomposition-like tool," *Appl. Comput. Harmon. Anal.*, vol. 30, no. 2, pp. 243–261, Mar. 2011.

[21] A. Ahrabian, D. Looney, L. Stanković, and D. P. Mandic, "Synchrosqueezing-based time-frequency analysis of multivariate data," *Signal Process.*, vol. 106, pp. 331–341, Jan. 2015.

[22] Y. Hu, X. Tu, and F. Li, "High-order synchrosqueezing wavelet transform and application to planetary gearbox fault diagnosis," *Mech. Syst. Signal Process.*, vol. 131, pp. 126–151, Sep. 2019.

[23] C. Li and M. Liang, "Time-frequency signal analysis for gearbox fault diagnosis using a generalized synchrosqueezing transform," *Mech. Syst. Signal Process.*, vol. 26, pp. 205–217, Jan. 2012.

[24] G. Kong and V. Koivunen, "Radar waveform recognition using Fourier-based synchrosqueezing transform and CNN," in *Proc. IEEE 8th Int. Workshop Comput. Adv. Multi-Sensor Adapt. Process. (CAMSAP)*, Dec. 2019, pp. 664–668.

[25] J. W. Pitton, L. E. Atlas, and P. J. Loughlin, "Applications of positive time-frequency distributions to speech processing," *IEEE Trans. Speech Audio Process.*, vol. 2, no. 4, pp. 554–566, 1994.

[26] T. Oberlin, S. Meignen, and V. Perrier, "Second-order synchrosqueezing transform or invertible reassignment? Towards ideal time-frequency representations," *IEEE Trans. Signal Process.*, vol. 63, no. 5, pp. 1335–1344, Mar. 2015.

[27] D.-H. Pham and S. Meignen, "High-order synchrosqueezing transform for multicomponent signals analysis—With an application to gravitational-wave signal," *IEEE Trans. Signal Process.*, vol. 65, no. 12, pp. 3168–3178, Jun. 2017.

[28] G. Yu, Z. Wang, and P. Zhao, "Multisynchrosqueezing transform," *IEEE Trans. Ind. Electron.*, vol. 66, no. 7, pp. 5441–5455, Jul. 2019.

[29] D. He, H. Cao, S. Wang, and X. Chen, "Time-reassigned synchrosqueezing transform: The algorithm and its applications in mechanical signal processing," *Mech. Syst. Signal Process.*, vol. 117, pp. 255–279, Feb. 2019.

[30] G. Yu, Z. Wang, P. Zhao, and Z. Li, "Local maximum synchrosqueezing transform: An energy-concentrated time-frequency analysis tool," *Mech. Syst. Signal Process.*, vol. 117, pp. 537–552, Feb. 2019.

[31] Z. Li, J. Gao, H. Li, Z. Zhang, N. Liu, and X. Zhu, "Synchroextracting transform: The theory analysis and comparisons with the synchrosqueezing transform," *Signal Process.*, vol. 166, Jan. 2020, Art. no. 107243.

[32] J. Yang, L. Pu, Z. Wang, Y. Zhou, and X. Yan, "Fault detection in a diesel engine by analysing the instantaneous angular speed," *Mech. Syst. Signal Process.*, vol. 15, no. 3, pp. 549–564, May 2001.

[33] Y. Liu, J. Zhang, K. Qin, and Y. Xu, "Diesel engine fault diagnosis using intrinsic time-scale decomposition and multistage AdaBoost relevance vector machine," *Proc. Inst. Mech. Eng., C, J. Mech. Eng. Sci.*, vol. 232, no. 5, pp. 881–894, Mar. 2018.

FEI DONG is currently pursuing the Ph.D. degree in ships and ocean engineering with the School of Naval Architecture, Ocean and Energy Power Engineering, Wuhan University of Technology, Wuhan, China. His research interests include condition monitoring and fault diagnosis of marine diesel engine.

JIANGUO YANG received the B.Sc. degree from the Wuhan Institute of Water Engineering, in 1982, with a focus on marine internal combustion engines, and the M.E. degree, in 1987.

He is currently the Chief Professor and an Academic Leader of marine engineering with the National Key Discipline. He is a Ph.D. Tutor with the Wuhan University of Technology. He has long been engaged in ship power system detection, diagnosis and intelligent control, and vibration and noise control research. He has trained more than 40 Ph.D. and graduate students. He has published more than 20 SCI and EI papers. In the past five years, nearly 20 provincial and ministerial projects, such as the State and Ministry of Industry and Information Technology. He has been awarded the Second Prize from the National Technological Inventions and the First Prize from the Scientific and Technological Progress in Hubei Province. He is a member of the International Society of Turbine Engineering. He is the Vice-Chairperson of the Professional Committee for High Power Diesel Engines of the Chinese Society of Internal Combustion Engines and the Director of the Fault Diagnosis Branch of the Chinese Society of Vibration Engineering.

LEI HU is currently a Teacher of marine engineering and energy and power engineering with the School of Naval Architecture, Ocean and Energy Power Engineering, Wuhan University of Technology. He has chaired and participated in the National Defense Science and Engineering Commission, the Ministry of Industry and Information Technology, the National Natural Science Fund, provincial and ministerial key scientific research projects, and horizontal research projects. He has long been committed to the basic and applied research of monitoring and diagnosis, health state assessment and intelligent control of marine engines and power systems.

SICONG SUN is currently pursuing the Ph.D. degree in ships and ocean engineering with the School of Naval Architecture, Ocean and Energy Power Engineering, Wuhan University of Technology, Wuhan, China. His research interests include vibration noise reduction and condition monitoring of marine diesel engine.

YUNKAI CAI is currently a Postdoctoral Researcher with the School of Naval Architecture, Ocean and Energy Power Engineering, Wuhan University of Technology. His research interests include engine performance optimization and emission control.

• • •